IEEE Access
Multidisciplinary | Rapid Review | Open Access Journal

Received April 13, 2019, accepted May 19, 2019, date of publication May 23, 2019, date of current version June 10, 2019.

*Digital Object Identifier 10.1109/ACCESS.2019.2918614*

# Deployment Dynamics of Large Space Antenna and Supporting Arms

**SHAOLIN LU[1,2], XIAOZHI QI[1,3], YING HU[1], (Member, IEEE), BING LI[2], (Senior Member, IEEE), AND JIANWEI ZHANG[3], (Member, IEEE)**

[1]CAS Key Laboratory of Human-Machine Intelligence-Synergy Systems, Shenzhen Institutes of Advanced Technology, Chinese Academy of Sciences, Shenzhen 518055, China
[2]Harbin Institute of Technology at Shenzhen, Shenzhen 518055, China
[3]University of Hamburg, 22527 Hamburg, Germany

Corresponding author: Xiaozhi Qi (xz.qi@siat.ac.cn)

This work was supported in part by the National Natural Science Foundation of China under Grant 51705512 and Grant U1613201, in part by the Shenzhen Fundamental Research Funds under Grant JCYJ20170307170252420, Grant JCYJ20170413104438332, and Grant GJHZ20170313113529978, in part by the Shenzhen Key Laboratory Project under Grant ZDSYS201707271637577, and in part by the German Science Foundation (DFG) and National Science Foundation of China (NSFC) in project Crossmodal Learning under contract Sonderforschungsbereich Transregio 169.

**ABSTRACT** As an important instrument for air-to-ground communication, the large space deployable antenna plays an important role in driving technological innovation and has become a topic of interest for research scholars worldwide. A large-scale deployable ring truss is introduced in this paper, which is equipped with a complete rope-driven driving method and supplements a cable net system in forming a complete space antenna. The antenna supporting arm is a slender structure that exhibits a certain flexible deformation during the deployment process of the antenna. A dynamic deployment model of supporting arms based on the absolute node coordinate formulation is established. In addition, based on the Lagrange equation, dynamic equations of multibody systems, including equations describing friction and flexible cable nets, are built. Furthermore, the optimal deployment process law of the antenna is developed. Finally, the performance of the deployment process of the antenna supporting arms and space deployable antenna is analyzed by the numerical simulation, which lays a solid foundation for subsequent prototype development and control theory research.

**INDEX TERMS** Deployable antenna, antenna supporting arms, dynamic modeling, optimal planning, dynamic analysis.

## I. INTRODUCTION

With the continuous development of satellite mobile user terminals towards light weight and portability and the increasing demand for time-sensitive target monitoring, large-scale space deployable antennas have become the key technical equipment for meeting the requirements of high-orbit mobile communication and remote sensing [1], [2]. Design, analysis and test verification techniques have become the core technology that is urgently needed for the development of aerospace technology. The research shows that the signal gain and propagation distance of large-scale space antennas are positively correlated with the aperture of the antenna [3]. Therefore, the scale of the spacecraft antenna becomes increasingly large, and the structure is increasingly complicated. However, due to the limited size of the spacecraft, it is unable to meet the requirements of large-scale structures. Therefore, it is extremely urgent to study high-quality antenna structures with large scale and high folding ratios [4], [5].

Although many large-scale space antennas have been successfully launched [6]–[8], smoothly deployed, and assigned to in-orbit service, there are still many unresolved problems in the deployment process of the antenna and its supporting arms. There have been many cases in which the entire project failed due to the failure of the antenna to deploy [9]. For example, in 1981, the US FLTSATCOM-5 satellite antenna failed to adapt for its structural deformation during the deployment process; in 1999, the EGS antenna on the Russian Mir space station failed in its first test due to the failure of the

The associate editor coordinating the review of this manuscript and approving it for publication was Dimitris Anagnostou.

unlocking mechanism; the first in-orbit deployment experiment of Japan's ETS-VIII communications satellite antenna failed in 2006 due to the entanglement of the flexible cable network and the antenna mechanism [10]. Therefore, it is necessary to focus on the dynamics of the entire deployment process.

In the development of large-scale space antennas, researchers from various countries have performed much research on deployable antennas and their dynamics, covering different types and deployment methods. Mitsugi et al. established a multibody system dynamics equation including a reflective metal mesh, a cable net system and a deployable truss. The accuracy of the model was verified by experiments, and the conclusion was that dynamic modeling is an indispensable tool for studying low-cost space antennas [11]. Zhang et al. provided a dynamic analysis method for complex truss and cable net systems and established a dynamic model for cable net systems using the finite element concept. In addition, from an energy point of view of the truss system, the dynamic equations of the system are established by the Lagrange method. The two models are combined to form the multibody system dynamics modeling method, and the effectiveness of the method has been verified by experiments [12]. Li et al. conducted in-depth research on the dynamic modeling, solution and control of flexible nonlinear multibody systems of deployable antennas. A complete set of algorithmic processes was formed, and successful research results were achieved [13], [14]. Deng et al. conducted in-depth research on mechanism synthesis and topology analysis [15] and designed a variety of algorithms to optimize the configuration [16], which provided powerful guidance for the design and deployment process control of large space deployable trusses.

The author's research group has conducted much research on deployable structure in recent years, including configuration design [17]–[19], degree of freedom analysis [20], optimization design [21], and cable network system research [22]. The antenna studied in this paper is a new type of deployable ring truss designed by the author's research group [23]. The basic module of the annular truss is composed of a closed six-bar mechanism, and the adjacent modules share a common vertical bar and the slider to form a closed-loop truss system. The number of modules can be selected according to different requirements to form ring trusses with different calibers. Compared with the classic AstroMesh antenna truss in the United States, the ring truss used in this paper is superior in some evaluation indicators, such as the ratio of the truss folding height to the deployed diameter, the diameter ratio before and after the deployment, and the volume ratio before and after the deployment.

Based on the current research status, the dynamics of flexible supporting arms and deployable antennas is studied in this paper. The rest of the paper is organized as follows: Section II outlines the structure of the antenna system, its working principle and analyses the necessity of this paper. The dynamic modeling method of flexible antenna supporting arms is described, and the accuracy of the method is verified in section III. Section IV establishes the kinematics of the deployable antenna and a multibody system dynamics model of the antenna, including the friction and cable net system. Deployment process planning of the supporting arms and the antenna, numerical simulation and results analysis are performed in section V. Section VI is a summary of the full text.

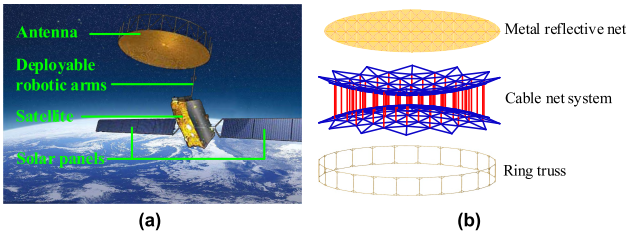


**FIGURE 1.** Schematic diagram of the spacecraft. (a) Spacecraft system. (b) Antenna components.

## II. OVERVIEW OF THE ANTENNA SYSTEM

### A. STRUCTURE OF THE ANTENNA SYSTEM

As an important medium for communication between space and earth, the spacecraft antenna structure has always been a topic of interest in various countries. As shown in Fig. 1(a), the communication satellite consists of three main components: the satellite body, solar panel and deployable antenna system. Among them, the deployable antenna system includes deployable supporting arms and a deployable antenna, and the research object of this paper is the complicated antenna system. The satellite body is the core of the entire spacecraft system, from which all the instructions are issued. Solar panels are mainly used to provide energy sources for the entire spacecraft. The deployable antenna is a tool for receiving and transmitting signals, as shown in Fig. 1(b), and consists of a ring truss, a cable net system and a metal reflective net. The metal reflective net is attached to the cable net system, and it is adjusted by the tension of the cable net system to achieve good profile accuracy.

### B. DEPLOYMENT PROCESS OF THE ANTENNA SYSTEM

The space deployable antenna is placed in the transmitter before being launched. After the transmitter reaches the designated altitude, the antenna system expands to its designated configuration in a specified order in which the truss antenna is deployed after the support arm is deployed. Specifically, the deployment process of antenna system includes several stages: 1) the arms are unlocked, and the "big arm" is extended by a certain angle of the motor; 2) the entire antenna system is rotated at a certain angle around the big arm's axis; 3) after the big arm is rotated into position, the "small arm" is unfolded to the designated position under the driving of the joint motor; 4) the reflector is unlocked and is positioned into the correct configuration by the driving system, then the reflector cable net system and the metal mesh are

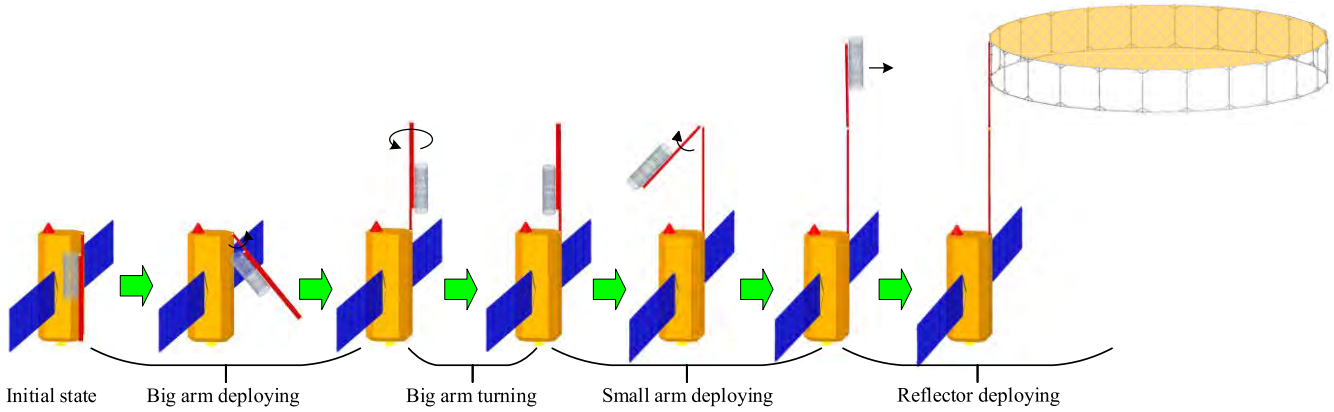


**FIGURE 2.** Deployment process of the antenna system.

promptly tightened to form a reflective paraboloid, as shown in Fig. 2.

The deployment process of the supporting arms is mainly driven by the motor, but the satellite space antenna consists of a large number of components, such as bars and motion pairs, and includes complex systems, such as flexible cable nets. Therefore, the deployment process and driving method of the antenna should be as simple as possible, and at the same time, the synchronous deployment requirements of the antenna should be satisfied, and a small number of motor drives should be used.

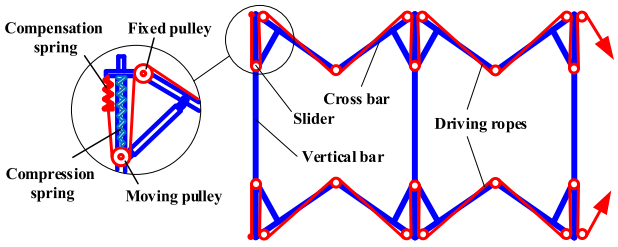


**FIGURE 3.** Schematic diagram of the deployment drive mode.

The deployment mode of ring antenna truss in this paper is driven by ropes. As shown in Fig. 3, two ropes are deployed on the upper and lower ends of the vertical bar. By pulling the slider to move to the upper and lower ends of the vertical bar, the crank slider mechanism is used to drive the crossbar to deploy so that the entire mechanism is deployed. The end of each driving rope contains a compensating spring whose main function is to avoid slack in the rope after unfolding the lock. Furthermore, a compression spring is mounted between the slider and the end of the vertical bar, the main function of which is to provide partial drive resistance, thereby avoiding slack in the driving rope during the deployment process.

Throughout the deployment process, there are many factors that could cause the deployment failure of the space antenna system [24], and the inaccurate dynamic modeling of the antenna deployment process is an important reason. The transformation of the large-space antenna structure from its initial collapsed state to full deployment to the working state in the space microgravity environment involves coupled motion of the spatial rigid body large-scale motion and elastic small deformation, which is a complex process with both linear and nonlinear aspects [25]. On the one hand, there are nonlinear factors such as the flexible cable net, joint clearance, friction, rod flexibility, and thermal alternating environment. On the other hand, the in-orbit deployment process of the antenna is coupled with the attitude control of the spacecraft, posing a potential threat to the attitude stability of the spacecraft body.

In addition, the ratio of the length of the antenna supporting arm to the diameter is large, associated with the elongated rod member, which exhibits a certain flexibility and elastic deformation during the deployment process. However, most researchers regard the antenna support arm as a rigid body, so that the deformation and vibration of supporting arm during the deployment process will not be discovered. Therefore, there is very little research in this area. The supporting arm does not affect the deployment of the antenna during deployment process since the antenna is always in the locked state. If the vibration of the supporting arm is too strong during the deployment process, it will affect the satellite body, which may cause the satellite body to be unstable or even reversed. Therefore, it is necessary to study the vibration of the supporting arm during deployment process to prevent a large impact on the satellite body.

## III. DYNAMIC MODELLING OF THE FLEXIBLE SUPPORTING ARMS

### A. DYNAMIC MODELLING BASED ON ABSOLUTE NODE COORDINATE FORMULATION

The absolute node coordinate formulation (ANCF) was proposed by Professor Ahmed A. Shabana in 1996 [26]. The analysis of a deformed flexible body is based on the theory of finite elements and continuum mechanics. ANCF modeling relies on a constant mass matrix, and there is no consideration of centrifugal force or Coriolis force, which is suitable to

describe the rigid motion of a flexible body. ANCF is considered to be one of the most important advances in the history of multibody system dynamics research.

The models before and after deformation of the beam element are shown in Fig. 4. The coordinates $\mathbf{r}$ of any point $P$ in the unit are expressed as follows,

$$\mathbf{r}_p = \begin{bmatrix} r_1 & r_2 \end{bmatrix}^T = \begin{bmatrix} X & Y \end{bmatrix}^T = \mathbf{Se} \tag{1}$$

where $\mathbf{S}$ is the shape function describing the deformation of the element and $\mathbf{e}$ is the generalized coordinate vector of the beam element node, which are defined as follows,

$$\mathbf{S} = \begin{bmatrix} S_1 & 0 & S_2 & 0 & S_3 & 0 & S_4 & 0 \\ 0 & S_1 & 0 & S_2 & 0 & S_3 & 0 & S_4 \end{bmatrix} \tag{2}$$

$$\begin{aligned} \mathbf{e} &= \begin{bmatrix} e_1 & e_2 & e_3 & e_4 & e_5 & e_6 & e_7 & e_8 \end{bmatrix}^T \\ &= \begin{bmatrix} r_{i1} & r_{i2} & \dfrac{\partial r_{i1}}{\partial x} & \dfrac{\partial r_{i2}}{\partial x} & r_{j1} & r_{j2} & \dfrac{\partial r_{j1}}{\partial x} & \dfrac{\partial r_{j2}}{\partial x} \end{bmatrix}^T \end{aligned} \tag{3}$$

In the shape function, $x$ is the local coordinate of point $P$, and $l$ is the length of the beam element, $\xi = x/l$, $S_1 = 1-3(\xi)^2+2(\xi)^3$, $S_2 = l\left(\xi - 2(\xi)^2 + (\xi)^3\right)$, $S_3 = 3(\xi)^2 - 2(\xi)^3$, $S_4 = l\left((\xi)^3 - (\xi)^2\right)$. In the generalized coordinate vector, $e_1$, $e_2$, $e_5$, *and* $e_6$ are the absolute coordinates of the two nodes $i$ and $j$, $e_3$, $e_4$, $e_7$, and $e_8$ are the slope components at the two nodes $i$ and $j$, which are tangent to the beam axis and perpendicular to the beam section normal. Therefore, in this model, the beam element adopts the Euler-Bernoulli assumption, that is, regardless of the shear deformation of the beam, only the bending deformation is considered, and the cross section is still a plane and perpendicular to the centerline of the beam.

The mass matrix based on ANCF can be obtained from the definition of beam energy. The kinetic energy $T$ of the beam element is defined as follows,

$$T = \frac{1}{2}\int_V \rho \dot{\mathbf{r}}^T \dot{\mathbf{r}} dV = \frac{1}{2}\dot{\mathbf{e}}^T \left[\int_V \rho \mathbf{S}^T \mathbf{S} dV\right] \dot{\mathbf{e}} \tag{4}$$

According to (4), the mass matrix $\mathbf{M}$ of the beam element can be obtained,

$$\mathbf{M} = \int_V \rho \mathbf{S}^T \mathbf{S}\, dV \tag{5}$$

It can be known from (5) that the mass matrix obtained based on ANCF is a constant matrix, which is related only to the length of the beam element and its own properties, which is an important feature of ANCF.

Under the action of gravity or external force, the flexible beam responds with elastic deformation and elastic force, as shown in Fig. 4. The strain energy produced by the deformation of the beam obtained from the continuum mechanical model is,

$$U = \frac{1}{2}\int_0^l EA\varepsilon_l^2 dx + \frac{1}{2}\int_0^l EI\kappa^2 dx \tag{6}$$

where $E$, $A$, $I$ represent the elastic modulus, cross sectional area and second moment of area, respectively. $\varepsilon_l$ represents the longitudinal strain of the beam bending and $\kappa$ represents the curvature. The two expressions are,

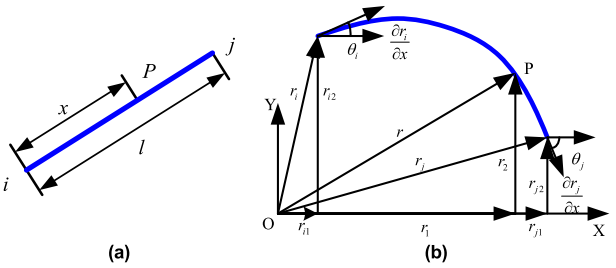


**FIGURE 4.** Shape of the beam element before and after deformation. (a) Before deformation. (b) After deformation.

$$\begin{cases} \varepsilon_l = \dfrac{1}{2}\left(\mathbf{e}^T \mathbf{S}'^T \mathbf{S}' \mathbf{e} - 1\right) \\ \kappa = \sqrt{\mathbf{e}^T \mathbf{S}''^T \mathbf{S}'' \mathbf{e}} \end{cases} \tag{7}$$

Find the two derivatives of the formula (6) to obtain the generalized stiffness matrix,

$$\mathbf{K} = \mathbf{K}_l + \mathbf{K}_n \tag{8}$$

where $\mathbf{K}_l$ and $\mathbf{K}_n$ are linear and nonlinear generalized stiffness matrices, respectively, which are calculated as follows,

$$\begin{cases} \mathbf{K}_l = \int_0^l EI\mathbf{S}''^T \mathbf{S}'' dx - \dfrac{1}{2}\int_0^l EA\mathbf{S}'^T \mathbf{S}' dx \\ \mathbf{K}_n = \dfrac{1}{2}\int_0^l EA(\mathbf{e}^T \mathbf{S}'^T \mathbf{S}'\mathbf{e})\mathbf{S}'^T \mathbf{S}' dx \end{cases} \tag{9}$$

The generalized external force and moment based on ANCF are also obtained according to the principle of virtual work [27]. Suppose a concentrated moment $\tau$ acts on the left $i$ or the right $j$ node of the beam element. The generalized external force vector corresponding to the external moment is,

$$\mathbf{Q} = \begin{cases} \begin{bmatrix} 0 & 0 & 0 & 0 & 0 & 0 & -\dfrac{\tau e_8}{f^2} & \dfrac{\tau e_7}{f^2} \end{bmatrix}^T, & \tau \text{ acts on left node } i \\ \begin{bmatrix} 0 & 0 & -\dfrac{\tau e_4}{f^2} & \dfrac{\tau e_3}{f^2} & 0 & 0 & 0 & 0 \end{bmatrix}^T, & \tau \text{ acts on right node } j \end{cases} \tag{10}$$

where $f = \sqrt{(\partial r_1/\partial x)^2 + (\partial r_2/\partial x)^2}$.

According to the mass matrix $\mathbf{M}$, the stiffness matrix $\mathbf{K}$, and the generalized external force $\mathbf{Q}$ obtained above, the kinematic equation obtained by ANCF is,

$$\mathbf{M}\ddot{\mathbf{q}} + \mathbf{Kq} = \mathbf{Q} \tag{11}$$

where $\ddot{\mathbf{q}}$ is the absolute acceleration vector, $\dot{\mathbf{q}}$ is the velocity vector, and $\mathbf{q}$ is the generalized node coordinate.

### B. SOLUTION OF THE DYNAMIC MODEL

The dynamic equation of the system is established according to ANCF. Considering the various constraints applying inside and outside the system, equation (11) cannot be directly solved. Therefore, various constraints are introduced into the

dynamic equation of the beam system. Using the Lagrange multiplier method [28], [29], the constraints are processed and introduced into the kinetic equation to obtain the following differential algebraic equations,

$$\begin{cases} \mathbf{M}\ddot{\mathbf{q}} + \Phi_{\mathbf{q}}^T \lambda = \mathbf{Q} - \mathbf{K}\mathbf{q} \\ \Phi(\mathbf{q}, t) = 0 \end{cases} \tag{12}$$

where, $\lambda$ is the Lagrange multiplier, $\Phi(\mathbf{q}, t)$ is the algebraic equation of the constraint, and $\Phi_{\mathbf{q}}$ is the Jacobian matrix of the constraint.

Then, $\Phi(\mathbf{q}, t)$ is differentiated twice with respect to time to obtain the differential algebraic equation of Index-1,

$$\begin{bmatrix} \mathbf{M} & \Phi_{\mathbf{q}}^T \\ \Phi_{\mathbf{q}} & 0 \end{bmatrix} \begin{bmatrix} \ddot{\mathbf{q}} \\ \lambda \end{bmatrix} = \begin{bmatrix} \mathbf{Q} - \mathbf{K}\mathbf{q} \\ -\Phi_{tt} - 2\Phi_{\mathbf{q}t}\dot{q} - \left(\Phi_{\mathbf{q}}\dot{q}\right)_{\mathbf{q}}\dot{q} \end{bmatrix} \tag{13}$$

After the dynamic equation is processed as described above, it becomes an ordinary differential equation and can be solved by a numerical algorithm. However, to avoid having to solve for the divergence, Baumgarte [30] proposed a constraint stability method based on the control feedback strategy, that is, the stability coefficient is introduced into the solution, resulting in the following form,

$$\begin{bmatrix} \ddot{\mathbf{q}} \\ \lambda \end{bmatrix} = \begin{bmatrix} \mathbf{M} & \Phi_{\mathbf{q}}^T \\ \Phi_{\mathbf{q}} & 0 \end{bmatrix}^{-1} \begin{bmatrix} \mathbf{Q} - \mathbf{K}\mathbf{q} \\ \gamma \end{bmatrix} \tag{14}$$

where $\gamma = -\Phi_n - 2\Phi_{qt}\dot{\mathrm{q}} - \left(\Phi_{\mathrm{q}}\dot{\mathrm{q}}\right)_{\mathrm{q}}\dot{\mathrm{q}} - 2\alpha\left(\Phi_{\mathrm{q}}\dot{\mathrm{q}} + \Phi_t\right) - \beta^2\Phi$ and where $\alpha$ and $\beta$ are stability factors. The range of $\alpha$ and $\beta$ is between 5 and 50. When $\alpha$ and $\beta$ reach a critical state, the response is stabilized relatively quickly. For the selection of $\alpha$ and $\beta$, refer to the related literature [31].

Assuming that the degree of freedom of the system is $n$, the first $n$ lines of equation (14) can be used to obtain the expression of $\ddot{\mathbf{q}}$, namely,

$$\ddot{\mathbf{q}} = \left( \begin{bmatrix} \mathbf{M} & \Phi_{\mathbf{q}}^T \\ \Phi_{\mathbf{q}} & 0 \end{bmatrix}^{-1} \begin{bmatrix} \mathbf{Q} - \mathbf{K}\mathbf{q} \\ \gamma \end{bmatrix} \right)_{1\sim n} \tag{15}$$

This formula can be solved by a variety of numerical methods.

### C. VERIFICATION OF THE DYNAMIC MODEL

The dynamics simulation process shown in Algorithm 1 is determined according to the dynamics modeling method described in the previous two sections.

The simulation process is evaluated for two cases of a single pendulum and double pendulum moving under the action of gravity, as shown in Fig. 5.

The attributes for the single pendulum and the double pendulum are shown in Table 1. Furthermore, the same model is established in Abaqus finite element software, and the accuracy of the above modeling process is verified by comparison of the results. For the above two simulation cases, as shown by the comparison results in Fig. 6, the results obtained by using the different modeling methods are extremely similar, so it can be proven that the dynamic model established by the absolute node coordinate method is correct and accurate.

**Algorithm 1** Multibody System Dynamics Modelling and Solution Based on ANCF

**Initialize:**
Initial Configuration, Element Information, Constant Matrices, Jacobian of Constraints
**Set**: stability factors $\alpha$ and $\beta$
**If** $\mathbf{q}$, $\dot{\mathbf{q}}$, and $\ddot{\mathbf{q}}$ have converged
**do:**
$t_{k+1} = t_k + \Delta t$
Calculate the elastic force $\mathbf{F}$
Calculate overall generalized external force $\mathbf{Q}$
Evaluate the integral for use in Eq. (15)
Update $\mathbf{q}$, $\dot{\mathbf{q}}$, $\ddot{\mathbf{q}}$, $k = k + 1$
**while** $k < n$
**Else**
return the '**Set**' statement, and reset the stability factors
**Output** the simulation results, and store the data
**End**

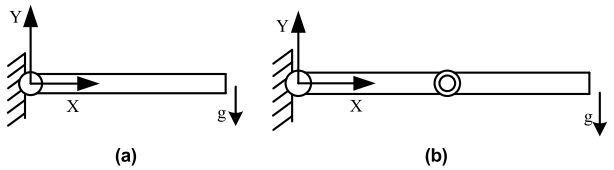


**FIGURE 5.** Diagram of the simulation model. (a) Single pendulum. (b) Double pendulum.

**TABLE 1.** Simulation parameters.

| Attributes | Simple pendulum | Double pendulum |
|---|---|---|
| Length (m) | 1.2 | 3.6 |
| Cross-sectional area ($m^2$) | 0.0018 | 0.00025 |
| Elastic modules (Pa) | $2\times10^9$ | $6.895\times10^{10}$ |
| Second moment of area ($m^4$) | $1.215\times10^{-8}$ | $1.302\times10^{-9}$ |
| Density ($kg/m^3$) | 5540 | 2770 |
| Simulation time (s) | 1.3 | 5 |
| Gravity acceleration ($m/s^2$) | 9.81 | |

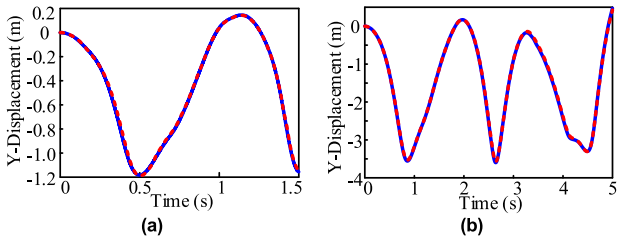


**FIGURE 6.** Simulation results in the Y direction. The blue solid line represents the simulation results with ANCF, and the red dotted line represents the simulation results with ABAQUS. (a) Single pendulum. (b) Double pendulum.

## IV. DYNAMIC MODELLING OF THE RING ANTENNA

### A. KINEMATIC MODEL

The kinematic model of the ring truss is established in this section. Due to the complex structure of the ring truss antenna, the model needs to be simplified before the

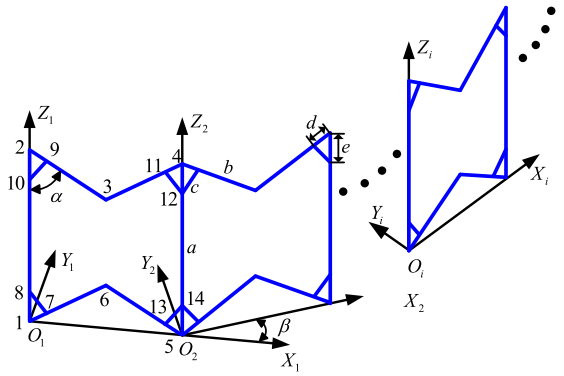


**FIGURE 7.** Ring antenna coordinate system. The numbers represent the joint nodes, the lowercase letters represent the length of the rod, and the uppercase letters represent the coordinate axes.

kinematic modeling. As shown in Fig. 7, the link is equivalent to a line segment, and the joint is equivalent to a node with numbers 1 to 14, ignoring the influence of other factors. The lever member $L_{12}$ is a vertical bar that is in contact with the antenna supporting arm and is regarded as a fixed lever here, and the remaining members are movable bars. Taking the line segment of $L_{12}$ as the Z-axis, the line where point 1 and its adjacent vertical rod's end point are located is the X-axis, and the Y-axis is determined according to the right-hand rule, so the coordinate system $O_1 - X_1Y_1Z_1$ is established and regarded as the basic coordinate system in the same manner. The local coordinate system $O_i - X_iY_iZ_i$ of each unit is sequentially established in a counter clockwise order. The angle between the X-axis of the adjacent local coordinate system is $\beta = 360°/n$, where $n$ is the number of modules.

Each rod has a fixed length of $a$, $b$, $c$, or $d$, as shown in Fig. 7. Furthermore, the distance from the moving slider to the end of the vertical rod is set to $e$, and the length is determined according to the triangular cosine theorem,

$$e = l_{1,8} = l_{2,10} = l_{4,12} = l_{5,14} = c\cos\alpha + \sqrt{d^2 - c^2\sin^2\alpha} \tag{16}$$

The antenna mechanism has a single global degree of freedom by the constraint of the double crank slider and the driving rope. Therefore, the spatial coordinates of each node can be uniquely represented at any time during the unfolding process and related only to the deployment angle $\alpha$.

Let $\mathbf{u}_i$ represent the spatial coordinates of each node $i$ in the unit, let $B$ be any point on any link $(j, k)$, and let the distance between $B$ and point $j$ be $x$. Then, the position of point $B$ in the global coordinate system can be expressed as,

$$\mathbf{r}_B = (x_B, y_B, z_B)^T = \mathbf{A}_i + \mathbf{R}_i \begin{bmatrix} 1 - \dfrac{x}{l_{j,k}} & \dfrac{x}{l_{j,k}} \end{bmatrix} \begin{bmatrix} \mathbf{u}_j \\ \mathbf{u}_k \end{bmatrix} \tag{17}$$

where $\mathbf{A}_i$ is the coordinate of the origin of the unit local coordinate system in the global coordinate system and $\mathbf{R}_i$ is the rotation matrix of the unit local coordinate relative to the global coordinate, respectively expressed as,

$$\mathbf{A}_i = \begin{cases} \begin{bmatrix} 0 & 0 & 0 \end{bmatrix}^T, & i = 1 \\ 2b\sin\alpha \begin{bmatrix} \sum_{j=2}^{i} \cos\left[(j-2)\beta\right] & \sum_{j=2}^{i} \sin\left[(j-2)\beta\right] & 0 \end{bmatrix}^T, & i \geq 2 \end{cases} \tag{18}$$

$$\mathbf{R}_i = \begin{bmatrix} \cos\left[(i-1)\beta\right] & -\sin\left[(i-1)\beta\right] & 0 \\ \sin\left[(i-1)\beta\right] & \cos\left[(i-1)\beta\right] & 0 \\ 0 & 0 & 1 \end{bmatrix} \tag{19}$$

Through the above formulas, the spatial position of any point on each rod in the global coordinate system can be obtained.

The deployment of the antenna mechanism requires actuation of the rope. Therefore, it is necessary to establish the relationship between the length of the rope and the deployment angle. Each rope in each module has 4 segments. Therefore, the total length of a single truss driving rope is,

$$L = 2n\,(2e + 2b) = 2n\left(c\cos\alpha + \sqrt{d^2 - c^2\sin^2\alpha} + b\right) \tag{20}$$

The velocity and acceleration information during the antenna deployment process can be obtained from the first and second derivatives of (17). The rope contraction speed and acceleration during the deployment process of the ring truss can be obtained by using the first and second derivatives, respectively, from (20).

### B. KINETIC ENERGY AND POTENTIAL ENERGY

The satellite space antenna system consists of key components such as a ring truss, driving ropes, cable net system and pulleys. The driving rope and cable net system are relatively light in weight and slow in speed, so their kinetic energy is neglected. The kinetic energy of the ring truss and joints is mainly studied.

According to the kinematic relationship established, for any rod in the ring truss, the linear density is $\rho$, and the position vector of any point $B$ on the rod in the global coordinate system $O_1 - X_1Y_1Z_1$ is $\mathbf{r}_B$. Perform line integration to obtain the kinetic energy of the rod,

$$E_e = \int_0^{l_e} \frac{1}{2}\rho\dot{\mathbf{r}}_B^T\dot{\mathbf{r}}_B dx \tag{21}$$

Therefore, the kinetic energy expression for a ring truss system with $n$ modules is,

$$E = \sum_{i=1}^{n}\left(\sum_{e=1}^{10} E_e + \sum_{j=1}^{14} E_j\right) = \frac{1}{2}J_\alpha\dot{\alpha}^2 \tag{22}$$

where $E_e$ and $E_j$ respectively represent the kinetic energy of the rod and joint, and $J_\alpha$ is the equivalent moment of inertia

of the system and can be expressed by

$$J_\alpha = \sum_{i=1}^{n}\sum_{e=1}^{10}\left(m_e\left(\left|\frac{\partial \mathbf{A}_i}{\partial\alpha}\right|^2 + \left(\frac{\partial \mathbf{A}_i}{\partial\alpha}\right)^T \mathbf{R}_i\left(\frac{\partial \mathbf{u}_j}{\partial\alpha}+\frac{\partial \mathbf{u}_k}{\partial\alpha}\right) + \frac{1}{3}\left(\left|\frac{\partial \mathbf{u}_j}{\partial\alpha}\right|^2 + \frac{\partial \mathbf{u}_j}{\partial\alpha}\cdot\frac{\partial \mathbf{u}_k}{\partial\alpha} + \left|\frac{\partial \mathbf{u}_k}{\partial\alpha}\right|^2\right)\right)\right) + \sum_{i=1}^{n}\sum_{j=1}^{14} m_j\left(\left|\frac{\partial \mathbf{A}_i}{\partial\alpha}\right|^2 + 2\left(\frac{\partial \mathbf{A}_i}{\partial\alpha}\right)^T \mathbf{R}_i\frac{\partial \mathbf{u}_j}{\partial\alpha} + \left|\frac{\partial \mathbf{u}_j}{\partial\alpha}\right|^2\right) \tag{23}$$

where $m_e$ is the mass of the bar and $m_j$ is the concentrated mass of the joint.

Since the antenna deployment is carried out in space, its gravitational potential energy is ignored. The main source of potential energy of the system is the cable net system and springs. According to Fig. 3, there is a compensating spring at the end of the driving rope, which is essentially rigid and undergoes little deformation during the deployment process; thus, its elastic potential is ignored. In addition, the ring truss contains a total of $2n$ compression springs. Ideally, all compression springs have the same deformation during the deployment process, with a stiffness coefficient of $k_1$ and a length of $l_0$ in the natural slack state; during the deployment process, the length is the distance $e$. The potential energy of the compression spring during the deployment process is,

$$U_1 = nk_1\left(l_0 - e\right)^2 \tag{24}$$

The system cable net is connected to the upper and lower ends of each vertical rod and is in a relaxed state at the initial stage of the deployment process. When deployed to a certain extent, the cable net system is gradually tightened until it is fully deployed. The cable net system has many cable segments and is intricate. This arrangement is equivalent to a plurality of springs with a stiffness of $k_2$ connected to the ring truss, where different styles of antennas get different stiffness $k_2$ by experiment. A model is shown in Fig. 8.

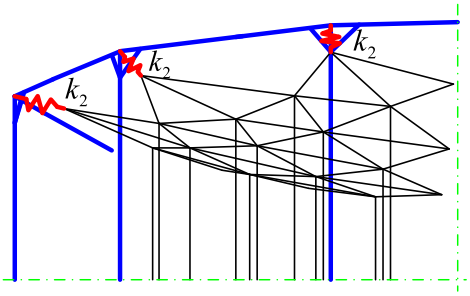


**FIGURE 8.** Schematic diagram of the cable-spring equivalent model. The blue line represents the ring truss, the black line represents the cable net system, and the red line represents the equivalent spring.

When the deployment angle of the mechanism is $\alpha_\mathbf{c}$, the cable net is in a critical tension state, and the deployment radius of the ring truss is $R$, the deployment radius of the cable net is $R_c$. As the deployment angle continues to increase, the potential energy of the entire cable network system is,

$$\begin{aligned} U_2 &= 2n\int_{R_c}^{R} k_2\left(R - R_c\right)dR \\ &= \frac{nk_2b^2\left(\sin\alpha - \sin\alpha_c\right)^2}{\sin^2\left(180^\circ/n\right)}, \quad \alpha \geq \alpha_c \end{aligned} \tag{25}$$

In summary, the system potential energy change function of the antenna during the deployment process is,

$$U = \begin{cases} nk_1\left(l_0 - e\right)^2, & 0 \leq \alpha < \alpha_c \\ nk_1\left(l_0 - e\right)^2 + \dfrac{nk_2b^2(\sin\alpha - \sin\alpha_c)^2}{\sin^2(180^\circ/n)}, & \alpha \geq \alpha_c \end{cases} \tag{26}$$

### C. SYSTEM GENERALIZED FORCE

The system generalized force mainly considers nonconservative forces, including the viscous friction of the joint, the control force of the motor on the driving rope, and the sliding friction between the rope and the pulley.

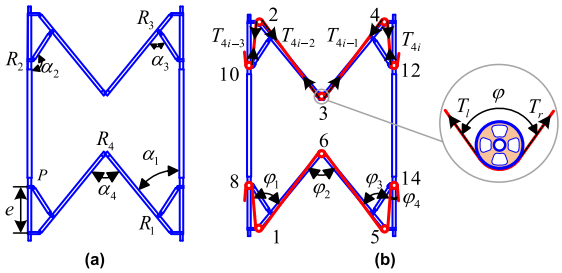


**FIGURE 9.** Basic structure and parameters an individual module. (a) Joint arrangement. (b) Rope tension diagram.

First, the viscous friction of each joint is considered. As shown in Fig. 9 (a), the single module contains four kinds of rotating joints and one kind of sliding joint. The viscous friction force is determined by the relative motion speed at both ends of the joint and the friction coefficient. The joint frictional friction $Q_f$ in the system is,

$$Q_f = -n\left(4\xi_1\dot{\alpha}_1\frac{\partial\alpha_1}{\partial\alpha} + 4\xi_1\dot{\alpha}_2\frac{\partial\alpha_2}{\partial\alpha} + 4\xi_1\dot{\alpha}_3\frac{\partial\alpha_3}{\partial\alpha} + 2\xi_1\dot{\alpha}_4\frac{\partial\alpha_4}{\partial\alpha}\right) - 2n\xi_2\dot{e}\frac{\partial e}{\partial\alpha} \tag{27}$$

where $\xi_1$ and $\xi_2$ is the viscous friction coefficient of the rotating joint and the sliding joint; $\alpha_1, \alpha_2, \alpha_3, \alpha_4$, and $e$ are the joint variables of the rotating joint and the sliding joint, which can be expressed as $\alpha_1 = \alpha$, $\alpha_2 = \pi - \arcsin\left(c\sin\alpha/d\right)$, $\alpha_3 = \alpha + \arcsin\left(c\sin\alpha/d\right)$, $\alpha_4 = 2\alpha$, and $e = c\cos\alpha + \sqrt{d^2 - c^2\sin^2\alpha}$.

Second, the generalized forces caused by the driving rope must be considered. According to the literature [32], for a rope pulley system containing friction, as shown in the partial view at joint 3 in Fig. 9 (b), the relationship between the rope tension on the left $T_l$ and right $T_r$ sides of the pulley is,

$$T_r = T_l e^{-\mu(\pi - \varphi)} \tag{28}$$

where $\mu$ represents the relative friction coefficient between the pulley and the rope. For each of the single ropes shown

in Fig. 9 (b), there are four sections. For each pulley, the rope tension decreases by a certain value. Therefore, the corresponding rope tension changes as follows,

$$\begin{cases} T_{4i-3} = T_{4i-4}e^{-\mu(\pi-\varphi_4)} = T_1 e^{-4\mu(i-1)(\pi-\alpha)} \\ T_{4i-2} = T_{4i-3}e^{-\mu(\pi-\varphi_1)} = T_1 e^{-4\mu(i-1)(\pi-\alpha)-\mu(\pi-\alpha)} \\ T_{4i-1} = T_{4i-2}e^{-\mu(\pi-\varphi_2)} = T_1 e^{-4\mu(i-1)(\pi-\alpha)-\mu(2\pi-3\alpha)} \\ T_{4i} = T_{4i-1}e^{-\mu(\pi-\varphi_3)} = T_1 e^{-4\mu(i-1)(\pi-\alpha)-\mu(3\pi-4\alpha)} \end{cases} \tag{29}$$

where $T_1$ is the driving force of the motor for single rope. The generalized force of the cable tension $T_{4i-3}$ to node 10 is,

$$\begin{aligned} Q_{10} &= \frac{T_{4i-3}}{|\mathbf{r}_2 - \mathbf{r}_{10}|}(\mathbf{r}_2 - \mathbf{r}_{10})^T \frac{\partial \mathbf{r}_{10}}{\partial \alpha} \\ &= \frac{T_{4i-3}}{|\mathbf{u}_{10,2}|}(\mathbf{u}_{10,2})^T \left(\frac{\partial \mathbf{u}_{10}}{\partial \alpha} + \mathbf{R}_i^T \frac{\partial \mathbf{A}_i}{\partial \alpha}\right) \end{aligned} \tag{30}$$

where $\mathbf{u}_{10,2} = \mathbf{u}_2 - \mathbf{u}_{10}$.

Similarly, the generalized force of the cable tension $T_{4i-3}$ on node 2 is,

$$Q_2 = \frac{T_{4i-3}}{|\mathbf{u}_{2,10}|}(\mathbf{u}_{2,10})^T \left(\frac{\partial \mathbf{u}_2}{\partial \alpha} + \mathbf{R}_i^T \frac{\partial \mathbf{A}_i}{\partial \alpha}\right) \tag{31}$$

Then, the generalized force caused by the tension $T_{4i-3}$ of the cable segment (10-2) is,

$$\begin{aligned} Q_{T_{4i-3}} &= Q_{10} + Q_2 = -\frac{T_{4i-3}}{|\mathbf{u}_{10,2}|}(\mathbf{u}_{10,2})^T \frac{\partial \mathbf{u}_{10,2}}{\partial \alpha} = -T_{4i-3}\frac{\partial e}{\partial \alpha} \\ &= T_1 \left[c\sin\alpha + \frac{c^2 \sin 2\alpha}{2\sqrt{d^2 - c^2\sin^2\alpha}}\right] e^{-4\mu(i-1)(\pi-\alpha)} \end{aligned} \tag{32}$$

Similarly, the generalized force of the remaining three cable segments is,

$$\begin{cases} Q_{T_{4i-2}} = Q_2 + Q_3 = -\dfrac{T_{4i-2}}{|\mathbf{u}_{2,3}|}(\mathbf{u}_{2,3})^T \frac{\partial \mathbf{u}_{2,3}}{\partial \alpha} = 0 \\ Q_{T_{4i-1}} = Q_3 + Q_4 = -\dfrac{T_{4i-1}}{|\mathbf{u}_{3,4}|}(\mathbf{u}_{3,4})^T \dfrac{\partial \mathbf{u}_{3,4}}{\partial \alpha} = 0 \\ Q_{T_{4i}} = Q_4 + Q_{12} = -\dfrac{T_{4i}}{|\mathbf{u}_{4,12}|}(\mathbf{u}_{4,12})^T \dfrac{\partial \mathbf{u}_{4,12}}{\partial \alpha} = -T_{4i}\dfrac{\partial e}{\partial \alpha} \\ \quad = T_1 \left[c\sin\alpha + \dfrac{c^2 \sin 2\alpha}{2\sqrt{d^2 - c^2\sin^2\alpha}}\right] \\ \qquad \times e^{-4\mu(i-1)(\pi-\alpha)-\mu(3\pi-4\alpha)} \end{cases} \tag{33}$$

Therefore, the generalized force $Q_T$ caused by the two driving ropes of the whole system is,

$$\begin{aligned} Q_T &= 2\sum_{i=1}^{n}\left(Q_{T_{4i-3}} + Q_{T_{4i-2}} + Q_{T_{4i-1}} + Q_{T_{4i}}\right) \\ &= 2T_1\left(c\sin\alpha + \frac{c^2\sin 2\alpha}{2\sqrt{d^2 - c^2\sin^2\alpha}}\right) \\ &\quad \times \sum_{i=1}^{n}\left[e^{-4\mu(i-1)(\pi-\alpha)}\left(1 + e^{-\mu(3\pi-4\alpha)}\right)\right] \end{aligned} \tag{34}$$

It can be seen from the above formula that the generalized force caused by the tension of the driving rope is related only to the variable angle $\alpha$ of deployment, so it can be written as,

$$Q_T = T_1 f(\alpha) \tag{35}$$

Finally, combine the generalized force caused $Q_\alpha$ by the viscous friction of the joint with the generalized force caused by the driving rope,

$$Q_\alpha = Q_f(\alpha, \dot{\alpha}) + Q_T(\alpha) \tag{36}$$

The above formula provides the generalized force of the system.

### D. DYNAMIC MODEL

The system kinetic energy, system potential energy and system generalized force obtained above are brought into the Lagrange dynamic equation to obtain,

$$\frac{d}{dt}\left(\frac{\partial(E-U)}{\partial \dot{\alpha}}\right) - \frac{d}{d\alpha}(E-U) = Q_f + Q_T \tag{37}$$

According to the formula described above, the upper potential energy $U$ and $J_\alpha$ of the kinetic energy $E$ are related only to the expansion angle $\alpha$, so (37) can be simplified as,

$$J_\alpha \ddot{\alpha} + \frac{1}{2}\frac{\partial J_\alpha}{\partial \alpha}\dot{\alpha}^2 + Q_f + \frac{\partial U}{\partial \alpha} - T_1 f(\alpha) = 0 \tag{38}$$

Equation (38) is the dynamic equation of the deployment process of the ring truss antenna. According to this equation, the rope driving force can be obtained by using the planned deployment method to obtain the control model.

## V. NUMERICAL SIMULATION AND RESULT ANALYSIS

### A. DEPLOYMENT PROCESS PLANNING OF THE ANTENNA SYSTEM

The deployment process of the supporting arms is planned first. Here, the main consideration is the flexibility of the arms, so the deployment phase of two arms is mainly planned.

During the deployment process, the antenna is considered to be a particle with a concentrated mass attached to the end of the support arms. In order to avoid the system impact problem near the locking time point during the deployment process of the antenna supporting arms, it is generally required that the relative speed of the arm approaches zero near the locking time point; otherwise, the satellite body will be impacted. The antenna supporting arm deployment process is planned using linear torque. Through multiple simulation experiments, a set of feasible arm driving torque functions is obtained, as shown in Fig. 10. The performance analysis of the supporting arm deployment process in the subsequent section is carried out under the action of the abovementioned driving torque.

After the arm is deployed, the focus shifts to the planning of the deployment process of the ring antenna. The kinematic relationship of the ring antenna is used to convert the angular velocity and angle into the displacement of the rope. Finally, the truss is deployed according to the predetermined plan by the control of the motor.

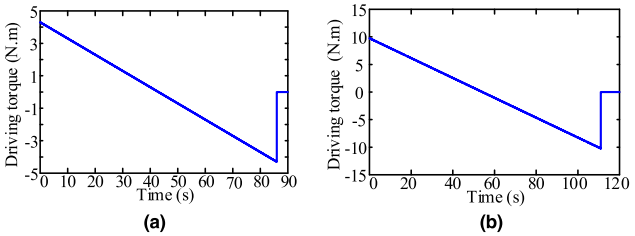


**FIGURE 10.** Deployment process planning of the supporting arms. (a) Deployment driving torque of the big arm. (b) Deployment driving torque of the small arm.

The first method uses a fifth-order polynomial function curve. In order to obtain the continuous deployment trajectory of the acceleration and to ensure that the specified position can be reached at the initial and final time points and that the speed meets requirements, a polynomial curve of order five is used here to plan the angular velocity during the expansion process to ensure a smooth deployment and to reduce chattering. The fifth-order polynomial function is defined as,

$$\begin{aligned} &Step5\left(x, x_0, h_0, x_1, h_1\right) \\ &= h_0+\left(h_1-h_0\right)\left[\left(x-x_0\right) / \left(x_1-x_0\right)\right]^3 \\ &\quad \cdot\left\{10-15\left[\left(x-x_0\right) / \left(x_1-x_0\right)\right]+6\left[\left(x-x_0\right) / \left(x_1-x_0\right)\right]^2\right\} \end{aligned} \tag{39}$$

where $x$ is the time variable, $x_0$ and $x_1$ are the start and end times, $h_0$ and $h_1$ are the function values corresponding to the start and end times, respectively.

The acceleration-deceleration deployment strategy is used to plan the deployment angular velocity $\dot{\alpha}$ as,

$$\dot{\alpha}=\begin{cases} Step5\left(t, 0, 0, T/2, \dot{\alpha}_1\right) & 0 \leq t \leq T/2 \\ Step5\left(t, T/2, \dot{\alpha}_1, T, 0\right) & T/2 \leq t \leq T \end{cases} \tag{40}$$

where $t$ is time, T is the total time of ring truss unfolding, and $\dot{\alpha}_1$ represents the deployment angular velocity at T/2. For time points within the range of 0∼T/2, the angular velocity of truss deployment increases gradually according to the fifth-order polynomial law. Within the range of T/2∼T, the angular velocity of the ring truss is reduced to zero according to the polynomial law. According to (40), it is necessary to satisfy $\alpha = \pi/\mathbf{2}$ when $t = T$, so $\dot{\alpha}_1 = (\pi - 2\alpha_0)/T$, which also represents the maximum speed of the deployment phase.

The second method uses a Bezier function curve. The Bezier function consists of control points and Bernstein basis functions. By defining the positions of several control points, a curve of arbitrary shape is obtained.

The deployment angle based on the Bezier function is defined as,

$$P(t)=\sum_{i=0}^{n} P_i B_{i,n}(t), \quad t \in [0, 1] \tag{41}$$

where $P(t)$ represents the deployment angle trajectory during the deployment process, $P_i$ represents the control point of the deployment process, and $B_{i,n}(t)$ is the Bernstein basis function of the Bezier function, which is defined as,

$$\begin{aligned} B_{i,n}(t) &= C_n^i t^i (1-t)^{n-i} \\ &= \frac{n!}{i!\,(n-i)!} t^i (1-t)^{n-i}, \quad t \in [0, 1] \end{aligned} \tag{42}$$

The velocity and acceleration can be derived from (41). In order to reduce the influence of the reaction force generated by the antenna, it is necessary to find a suitable set of solutions $\mathbf{P}_i$ to minimize the maximum value of the angular acceleration while satisfying the constraints of the angular velocity $\dot{P}(t)$ and the angular acceleration $\ddot{P}(t)$ continuity. Therefore, the optimization model is established as follows.

Find,

$$\mathbf{P}_i = \begin{pmatrix} P_0 & P_1 & \cdots & P_N \end{pmatrix}^T \tag{43}$$

subject to the objective function,

$$min \quad f = max(abs(\ddot{\mathrm{P}}(t))) \tag{44}$$

restricted to,

$$\begin{cases} P(0) = \alpha_0, & P(1) = \pi/2 \\ \dot{P}(0) = 0, & \dot{P}(1) = 0 \\ \ddot{P}(0) = 0, & \ddot{P}(1) = 0 \end{cases} \tag{45}$$

Here, an eighth-order Bezier function is established; find a suitable set of planning angles $\mathbf{P} = (0.0768, 0.0768, 0.0768, 0.4465, 0.8152, 1.2169, 1.5708, 1.5708, 1.5708)$ through the optimization algorithm, and apply the Bezier function to the set. The planned deployment angle, angular velocity, and angular acceleration are shown in Fig. 11 and compared with the results of the first planning method.

According to Fig. 11 (c), it can be found that the peak acceleration of the angular acceleration based on the Bezier function is $4.28 \times 10^{-4}$ rad/s$^2$, which is 24.6% lower than the peak acceleration of the angular acceleration $5.7 \times 10^{-4}$ rad/s$^2$ based on the fifth-order polynomial function, and the angular velocity of the expansion is also greatly reduced, which further reduces the impact of satellite truss unfolding on the ontology.

Based on the deployment law of Bezier function programming, the deployment trajectory of the rope is shown in Fig. 12. It can be seen from the figure that the peak of the rope contraction acceleration based on the Bezier function expansion is $2.51 \times 10^{-3}$m/s$^2$, which is 29.3% lower than the rope contraction acceleration peak $3.55 \times 10^{-3}$m/s$^2$ obtained from the fifth-order polynomial function. The performance is greatly improved, and the expansion of the ring truss can be well controlled by the motor.

By comparing the results of above two deployment planning, it is found that, compared with the fifth-order function expansion law, using the Bezier function law for planning further reduces the peak of the acceleration, thereby improving the deployment performance of the satellite truss. Therefore, using above-planned Bezier function expansion rule, through MATLAB programming, the truss deployment process can be

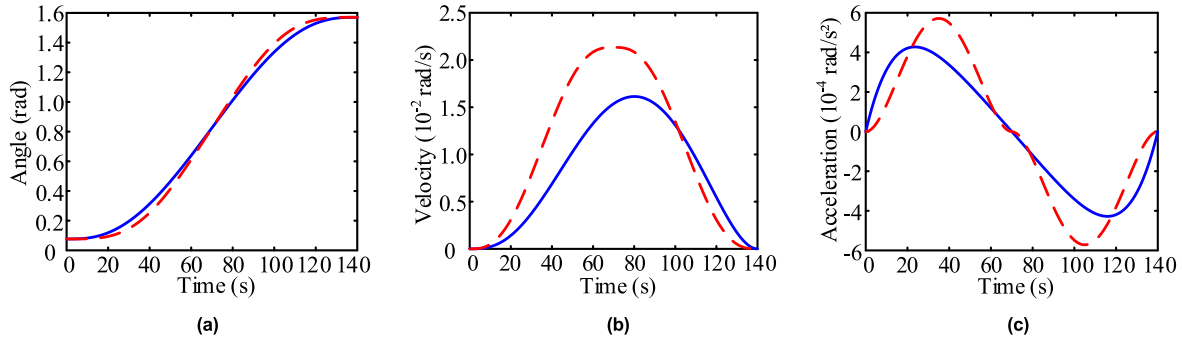


**FIGURE 11.** Comparison of two planning methods. The solid blue line represents the trajectory of the Bezier method planning, and the red dashed line represents the trajectory of the fifth-order polynomial function planning. (a) Angle. (b) Angular velocity. (c) Angular acceleration.

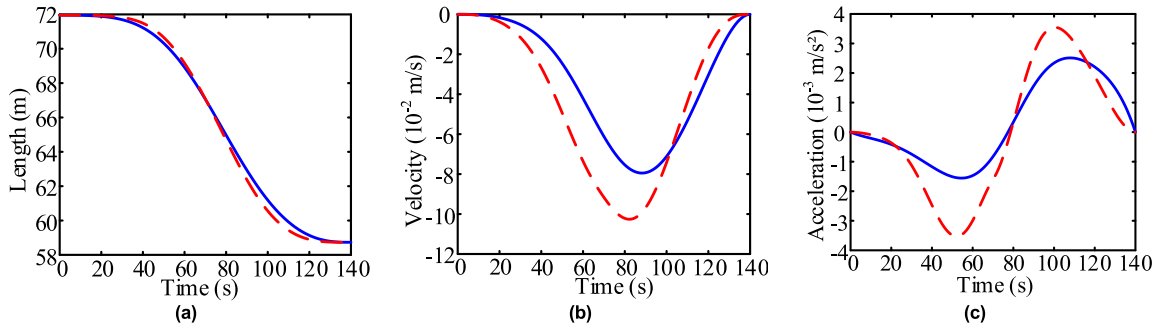


**FIGURE 12.** Planning the rope contraction parameters. The solid blue line represents the trajectory of the Bezier method planning, and the red dashed line represents the trajectory of the fifth-order polynomial function planning.(a) Length. (b) Speed. (c) Acceleration.

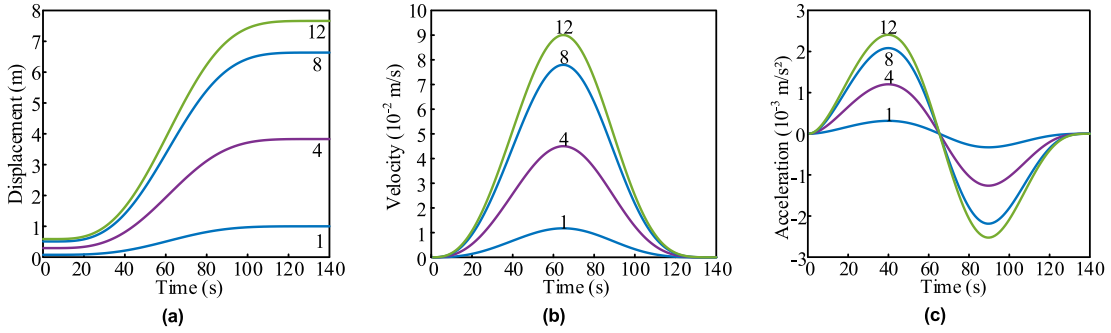


**FIGURE 13.** Simulation results of the motion of some bars based on Bezier planning. For clarity, and due to symmetry, take the 1st, 4th, 8th, and 12th poles of the 24 vertical bars. (a) Displacement change. (b) Speed change. (c) Acceleration change.

simulated, $a$ and $b$ are set to 1 m and 0.5 m correspondingly, and the parameter change are obtained as shown in Fig. 13.

As shown in Fig. 13, the displacement, velocity and acceleration of bars 1, 4, 8 and 12 are extracted. According to the Fig. 13 (a), the ring truss can be fully expanded from the initial angle of 4.4° to 90°. The truss extends 588 mm before unfolding; the diameter after unfolding is 7660 mm, the diameter ratio before and after unfolding is approximately 0.077, and the height-to-diameter ratio is 0.13. To increase the expansion diameter, simply increase the number of units. According to the speed curve of Fig. 13 (b), it can be found that by Bezier curve planning, the speed in the initial expansion phase increases steadily, and the maximum speed generation time appears in the middle and at the end of the expansion phase, smoothly approaching zero, which reduces the effects of vibrations generated during the process of deployment and locking to the satellite's body. Similarly, according to the deployment acceleration curve of Fig. 13 (c), it can be found that the accelerations are also close to zero at the initial stage and the end stage of the unfolding, thus avoiding impact vibration caused by inertia. The above results show that the planning method fully meets the optimization goals taken on at the beginning of this section. The antenna deployment process is shown in Fig. 14.

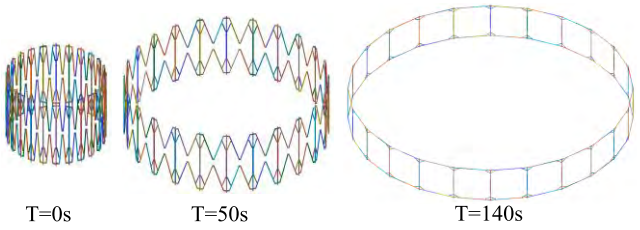


**FIGURE 14.** Schematic diagram of the antenna deployment process.

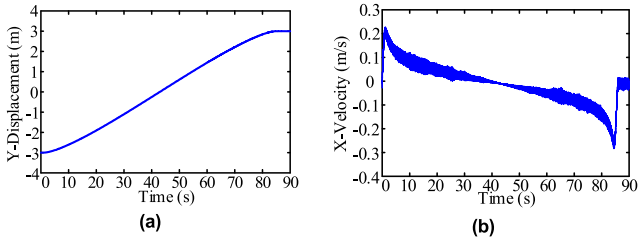


**FIGURE 15.** Deployment performance of the big arm. (a) Displacement of the big arm ending in the Y direction. (b) Speed of the big arm ending in the X direction.

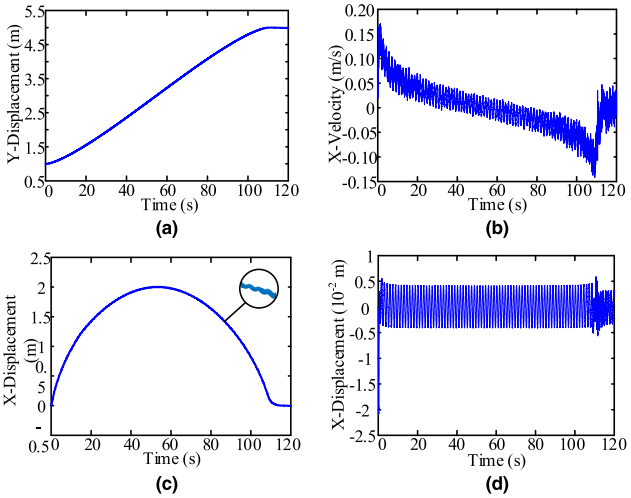


**FIGURE 16.** Deployment performance of the small arm. (a) Displacement of the end of the small arm in the Y direction. (b) Speed at the end of the small arm in the X direction. (c) Displacement of the end of the small arm in the X direction. (d) Drift at the end of the big arm in the X direction.

### B. ANALYSIS OF THE SUPPORTING ARM'S DEPLOYMENT PROCESS

The total length of the supporting arms is 5 m, of which the big arm extends 3 m and the small arm extends 2 m. According to the calculated driving torque of the big arm, the simulation results are shown in Fig. 15. It can be seen from Fig. 15(a) that at 86 s, the big arm is deployed in its ideal position. It can be seen from Fig. 15(b) that there is always a slight vibration during the deployment process of the arm. When the arm reaches its ideal position, it is slightly oscillating due to the elastic deformation. It can be seen from the simulation results that the vibration of the big arm is minimal during the entire deployment process.

After the big arm is deployed, the small arm is unlocked and begins to deploy. Under the driving of the linear moment shown in Fig. 10 (b), the deployment process of the small arm is as shown in Fig. 16. As shown in Fig. 16 (a), under the action of the linear driving torque, the small arm is deployed to a predetermined position at approximately 112 s. In this process, a more pronounced vibration is produced than that of the deployment process of the big arm, as shown in Fig. 16 (b) and Fig. 16 (c).

This result occurs because the driving of the arm is based on the end of the big arm, and the simulation result of the small arm deployment includes the superposition of the flexible deformation of the big and small arms, so the vibration amplitude at the end of the small arm is significantly increased, and the vibration frequency is significantly reduced. At the end of the deployment process, the lock-up time fluctuates greatly, and the fluctuation range is greater than that of the vibration amplitude during the deployment process. It can be seen from Fig. 16(d) that during the deployment process of the small arm, the end of the big arm produces a continuous positional drift, mainly caused by the reaction force generated by the deployment of the small arm, and the frequency of the big arm drift is consistent with the frequency of the vibration during the deployment process of the small arm.

From the entire deployment process of the antenna supporting arm, it can be found that vibration is generated both during the deployment process and at the time of locking; the amplitude and frequency of the low-order vibration of the antenna support arm during the rotation increases with the increase of the rotational speed, and this effect does not diminish as the expansion process progresses. This vibration affects the attitude stability of the satellite body, so it is necessary to design a more reasonable deployment mode when necessary and to design a stable controller to control the smooth deployment of the antenna supporting arms. Second, the vibration amplitude can be decreased by increasing its deployment time and reducing the rotation speed. In addition, the antenna support arms can be fabricated from a material with a larger modulus of elasticity to reduce the elastic deformation and vibration amplitude during the deployment process.

### C. DYNAMIC SUMULATION OF THE ANTENNA'S DEPLOYMENT PROCESS

Based on the Lagrange dynamics model established in the previous section, a program was developed to study the dynamic performance. The parameters are set as follows: geometric parameters of the ring truss $a = 1$ m, $b = 0.45$ m, $c = 0.1$ m, $d = 0.15$ m, number of truss modules studied $n = 24$, linear density of the bars $\rho = 1800$ kg/m$^3$, initial deployment angle $\alpha_0 = 4.4°$, critical angle of tensioning of cable net system $\alpha_c = 80°$, compression spring stiffness coefficient $k_1 = 100$ N/m, equivalent spring stiffness coefficient of the cable net system $k_2 = 200$ N/m, length of the compression spring in its natural state $l_0 = 0.3$ m, viscous friction coefficient of the rotating joint $\xi_1 = 0.1$, and viscous

friction coefficient of the sliding joint $\xi_2 = 0.1$. The dynamic performance is simulated in MATLAB.

First, the dynamic performance and energy relationship are studied when $\mu = 0$. At that time, regardless of the frictional relationship between the rope and the pulley, the tension over the entire driving rope is constant. The energy change diagram is shown in Fig. 17.

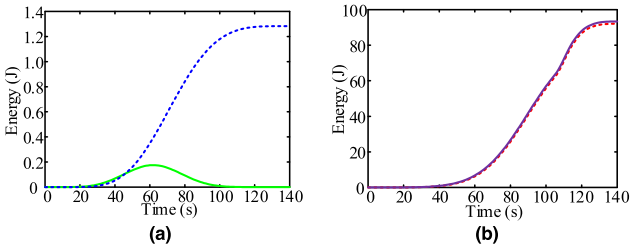


**FIGURE 17.** Energy change diagram when $\mu = 0$. In (a), the green solid line represents the system kinetic energy, and the blue dotted line represents the joint dissipative energy; in (b), the purple color represents the input work, and the red dotted line represents the system potential energy change. (a) Variation curve of the kinetic energy and joint dissipation energy. (b) Variation curve of the potential energy and input work.

As shown in Fig. 17, the energy change diagram at $\mu = 0$ shows that the absolute speed of the movement of the rod and the relative rotational speed of both sides of the joint is small during the whole deployment process. Therefore, the kinetic energy of the whole system and the joint dissipating energy are both very small. It can be seen from Fig. 17(b) that the input work of the motor is mainly converted into the potential energy of the compression spring. On the whole, the sum of the system kinetic energy, joint dissipative energy and system potential energy is equal to the motor input work, which is consistent with the law of conservation of energy, so it can be verified that the established dynamic model is correct.

There must be relative friction between the pulley and the driving rope, so the dynamic deployment performance is studied when $\mu = 0.01$. The energy relationship of the system is shown in Fig. 18. In this case, the input energy of the system is converted into kinetic energy, potential energy and joint dissipating energy, and the residual energy is lost by the friction between the pulley and the driving rope, which is in line with the law of conservation of energy.

Fig. 19 shows the variation of the output force of the motor with time under different friction coefficients $\mu$ based on the deployment law of the Bezier function. It can be seen that the trend of the output force of the motor is consistent under different friction coefficients. At the initial time point, because the compression spring is in a slightly compressed state, the driving rope has a certain tension. As the deployment process progresses, the output force of the motor gradually increases. When the cable net system is tightened, the load force of the motor increases, rapidly. Then, the deployment speed is gradually reduced, and the motor output force is rapidly reduced until the final motor output force needs to overcome only the resistance of the compression spring. This

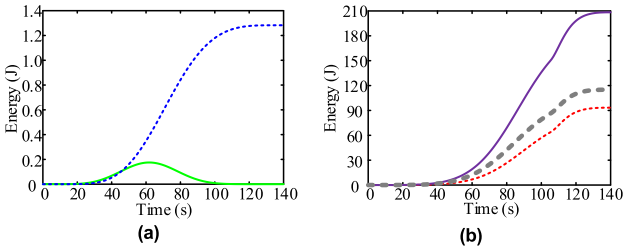


**FIGURE 18.** Energy change diagram when $\mu = 0$. In (a), the green solid line represents the system kinetic energy, and the blue dotted line represents the joint dissipative energy; in (b), the purple color represents the input work, the red dotted line represents the system potential energy change, and the gray bold dotted line represents the pulley dissipated energy. (a) Variation curve of the kinetic energy and joint dissipation energy. (b) Variation curve of the potential energy, pulley dissipation energy and input work.

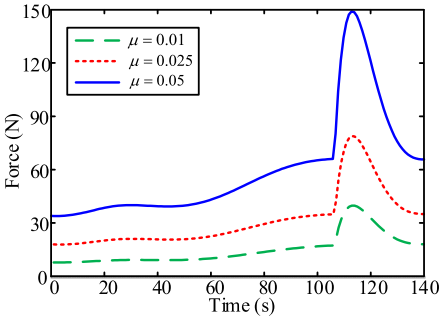


**FIGURE 19.** Motor output force under different friction coefficients.

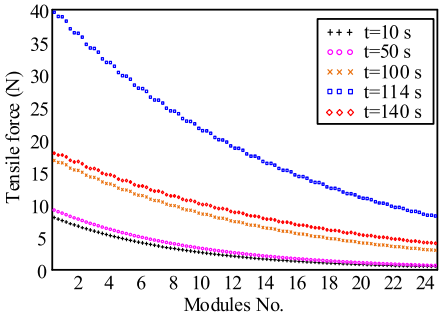


**FIGURE 20.** Tension values of different cable segments at different time.

is because the resistance of the cable net system is mostly carried by the ring truss at the end of the deployment process, and the motor output force needs to overcome only a small amount of resistance.

Upon full deployment, the ring truss reaches its singular point, the resistance of the cable net system is completely offset by the ring truss, and the motor does not have to bear the resistance of the cable net. This is an important advantage of this ring truss antenna. Therefore, it is necessary to select a material with a small relative friction coefficient in the selection of the driving rope and the pulley material to maximize the energy utilization rate.

Finally, due to the friction of the pulley, the driving force decreases every time a cable passes through a pulley, and the

divergence law is different due to the different wrap angles of the driving ropes on different pulleys, as shown in Fig. 20. The tension value of each cable segment at different times can be seen from the figure. The whole mechanism has a total of 24 modules, a total of 96 with the cable section. The tension of any individual cable section varies along the entire driving rope, with a downward trend following the motor output, and the tension of the rope segment farthest from the motor is the smallest.

## VI. CONCLUSION

The dynamics of the antenna and its supporting arms is presented and investigated in this paper. The deployment of the antenna supporting arm is an important part of spacecraft design, but it is also the most easily overlooked part. A new flexible body dynamics modeling method, ANCF, which has a constant mass matrix and does not incorporate a Coriolis force or centripetal force, is introduced in this paper. Based on this method, the dynamic model of the supporting arm is established, and the solution algorithm of the dynamic equation is designed. The accuracy of the model and the algorithm is verified by example cases. In addition, through a number of experiments, a linear driving torque that fully deploys the arm is obtained. Secondly, the article introduces a large truss recently developed by the authors' research group and proposes a complete rope-driving method of deployment. The generalized force of the driving rope is derived, and the dynamic kinetic energy and potential energy of the system are used to form the complete Lagrange multibody system dynamics equation, including the friction force for a flexible cable net. By comparing various deployment planning methods, the optimal deployment planning of the system is determined.

Simulation results show that the antenna supporting arm always undergoes high-frequency jitter during the deployment process, which is particularly obvious during the deployment of the arm and necessitates attention by researchers. The vibration of the supporting arm during the deployment process increase with increasing speed, and the frequency decreases with increasing arm length. In order to suppress this phenomenon, three reasonable measures are proposed in this paper. Moreover, through optimal deployment planning, the antenna can be deployed smoothly, minimizing the reaction force generated, thereby weakening the coupling effect between the satellite body and the antenna. In this process, the input power of the motor is mainly converted into the potential energy of the spring and the cable net system, and most of the remaining power is converted into the thermal energy of the driving system, while the kinetic energy is small; the whole system conforms to the principle of energy conservation. This article is of great significance for the development of the new type of ring truss antenna. In the future work, the flexibility of the ring truss and the joint clearance will be addressed to more accurately represent the real situation.

## REFERENCES

[1] J. Santiago-Prowald and H. Baier, "Advances in deployable structures and surfaces for large apertures in space," *CEAS Space J.*, vol. 5, nos. 3–4, pp. 89–115, 2013.
[2] Y. Rahmat-Samii and A. C. Densmore, "Technology trends and challenges of antennas for satellite communication systems," *IEEE Trans. Antennas Propag.*, vol. 63, no. 4, pp. 1191–1204, Apr. 2015.
[3] Y. Zhang, W. Ru, G. Yang, and N. Li, "Deployment analysis considering the cable-net tension effect for deployable antennas," *Aerosp. Sci. Technol.*, vol. 48, pp. 193–202, Jan. 2016.
[4] R. W. Thompson, A. W. Wilhite, D. Reeves, D. O. Stanley, and J. Wagner, "Mass growth in space vehicle and exploration architecture development," *Acta Astronautica*, vol. 66, nos. 7–8, pp. 1220–1236, Apr. 2010.
[5] L. Puig, A. Barton, and N. Rando, "A review on large deployable structures for astrophysics missions," *Acta Astronautica*, vol. 67, nos. 1–2, pp. 12–26, 2010.
[6] A. Meguro, K. Shintate, M. Usui, and A. Tsujihata, "In-orbit deployment characteristics of large deployable antenna reflector onboard engineering test satellite VIII," *Acta Astronautica*, vol. 65, nos. 9–10, pp. 1306–1316, 2009.
[7] M. Mobrem, S. Kuehn, C. Spier, and E. Slimko, "Design and performance of astromesh reflector onboard soil moisture active passive spacecraft," in *Proc. IEEE Aerosp. Conf.*, Mar. 2012, pp. 1–10.
[8] D. Semler, A. Tulintseff, R. Sorrell, and J. Marshburn, "Design, integration, and deployment of the terreStar 18-meter reflector," in *Proc. 28th AIAA Int. Commun. Satell. Syst. Conf. (ICSSC)*, Sep. 2010, p. 8855.
[9] M. Tafazoli, "A study of on-orbit spacecraft failures," *Acta Astronautica*, vol. 64, pp. 195–205, Jan./Feb. 2009.
[10] M. A. Wise, J. H. Saleh, and R. A. Haga, "Health scorecard of spacecraft platforms: Track record of on-orbit anomalies and failures and preliminary comparative analysis," *Acta Astronautica*, vol. 68, nos. 1–2, pp. 253–268, 2011.
[11] J. Mitsugi, K. Ando, Y. Senbokuya, and A. Meguro, "Deployment analysis of large space antenna using flexible multibody dynamics simulation," *Acta Astronautica*, vol. 47, no. 1, pp. 19–26, Jul. 2000.
[12] Y. Zhang, N. Li, G. Yang, and W. Ru, "Dynamic analysis of the deployment for mesh reflector deployable antennas with the cable-net structure," *Acta Astronautica*, vol. 131, pp. 182–189, Feb. 2017.
[13] P. Li, C. Liu, Q. Tian, H. Hu, and Y. Song, "Dynamics of a deployable mesh reflector of satellite antenna: Form-finding and modal analysis," *J. Comput. Nonlinear Dyn.*, vol. 11, no. 4, 2016, Art. no. 041017.
[14] P. Li, C. Liu, Q. Tian, H. Hu, and Y. Song, "Dynamics of a deployable mesh reflector of satellite antenna: Parallel computation and deployment simulation," *J. Comput. Nonlinear Dyn.*, vol. 11, no. 6, 2016, Art. no. 061005.
[15] C. Shi, H. Guo, Z. Zheng, M. Li, R. Liu, and Z. Deng, "Conceptual configuration synthesis and topology structure analysis of double-layer hoop deployable antenna unit," *Mech. Mach. Theory*, vol. 129, pp. 232–260, Nov. 2018.
[16] R. Liu, H. Guo, R. Liu, H. Wang, D. Tang, and Z. Deng, "Structural design and optimization of large cable–rib tension deployable antenna structure with dynamic constraint," *Acta Astronautica*, vol. 151, pp. 160–172, Oct. 2018.
[17] H. Huang, B. Li, T. Zhang, Z. Zhang, X. Qi, and Y. Hu, "Design of large single-mobility surface-deployable mechanism using irregularly shaped triangular prismoid modules," *J. Mech. Des.*, vol. 141, no. 1, 2019, Art. no. 012301.
[18] Z. Deng, H. Huang, B. Li, and R. Liu, "Synthesis of deployable/foldable single loop mechanisms with revolute joints," *J. Mech. Robot.*, vol. 3, no. 3, Aug. 2011, Art. no. 031006.
[19] G. Li, H. Huang, H. Guo, and B. Li, "Dynamic modeling and control for a deployable grasping manipulator," *IEEE Access*, vol. 7, pp. 23000–23011, 2019.
[20] X. Qi, H. Huang, Z. Miao, B. Li, and Z. Deng, "Design and mobility analysis of large deployable mechanisms based on plane-symmetric Bricard linkage," *J. Mech. Des.*, vol. 139, no. 2, 2017, Art. no. 022302.
[21] X. Qi, Z. Deng, B. Li, R. Liu, and H. Guo, "Design and optimization of large deployable mechanism constructed by Myard linkages," *CEAS Space J.*, vol. 5, nos. 3–4, pp. 147–155, 2013.
[22] Z. Chu, Z. Deng, X. Qi, and B. Li, "Modeling and analysis of a large deployable antenna structure," *Acta Astronautica*, vol. 95, pp. 51–60, Feb./Mar. 2014.
[23] X. Qi, H. Huang, B. Li, and Z. Deng, "A large ring deployable mechanism for space satellite antenna," *Aerosp. Sci. Technol.*, vol. 58, pp. 498–510, Nov. 2016.

[24] Y. Liu, S. B. Kim, A. Chattopadhyay, and D. T. Doyle, "Application of system-identification techniquest to health monitoring of on-orbit satellite boom structures," *J. Spacecraft Rockets*, vol. 48, no. 4, pp. 589–598, 2011.
[25] W. Xu, B. Liang, and Y. Xu, "Survey of modeling, planning, and ground verification of space robotic systems," *Acta Astronautica*, vol. 68, pp. 1629–1649, Jun./Jul. 2011.
[26] A. A. Shabana, "Flexible multibody dynamics: Review of past and recent developments," *Multibody Syst. Dyn.*, vol. 1, no. 2, pp. 189–222, Jun. 1997.
[27] J. L. Escalona, H. A. Hussien, and A. A. Shabana, "Application of the absolute nodal co-ordinate formulation to multibody system dynamics," *J. Sound Vib.*, vol. 214, no. 5, pp. 833–851, 1998.
[28] J. G. de Jalón and M. D. Gutiérrez-López, "Multibody dynamics with redundant constraints and singular mass matrix: Existence, uniqueness, and determination of solutions for accelerations and constraint forces," *Multibody Syst. Dyn.*, vol. 30, no. 3, pp. 311–341, 2013.
[29] R. A. Wehage and E. Haug, "Generalized coordinate partitioning for dimension reduction in analysis of constrained dynamic systems," *J. Mech. Des.*, vol. 104, no. 1, pp. 247–255, 1982.
[30] J. Baumgarte, "Stabilization of constraints and integrals of motion in dynamical systems," *Comput. Methods Appl. Mech. Eng.*, vol. 1, no. 1, pp. 1–16, Jun. 1972.
[31] S.-T. Lin and J.-N. Huang, "Stabilization of Baumgarte's method using the Runge–Kutta approach," *J. Mech. Des.*, vol. 124, no. 4, pp. 633–641, Nov. 2002.
[32] B. Li, X. Qi, H. Huang, and W. Xu, "Modeling and analysis of deployment dynamics for a novel ring mechanism," *Acta Astronautica*, vol. 120, pp. 59–74, Mar./Apr. 2016.

**SHAOLIN LU** received the B.S. degree from Nanjing Tech University, Nanjing, China, in 2017. He is currently pursuing the M.S. degree with the Harbin Institute of Technology at Shenzhen, Shenzhen, China.

He has been performing research as a Guest M.S. Student with the Shenzhen Institute of Advanced Technology, Chinese Academy of Sciences, since 2018. His research interests include space deployable mechanisms and nonlinear control.

**XIAOZHI QI** received the B.S. degree from Yanshan University, in 2009, and the M.S. and Ph.D. degrees from the Harbin Institute of Technology at Shenzhen, China, in 2011 and 2017, respectively.

He is currently a Postdoctoral Researcher with the University of Hamburg, Germany, and an Associate Professor with the Shenzhen Institutes of Advanced Technology, Chinese Academy of Sciences, China. His research interests include medical assistant robots and space deployable mechanisms.

**YING HU** (M'11) received the B.S. degree from Shanghai Jiaotong University, Shanghai, China, in 1991, and the M.S. and Ph.D. degrees in mechanical engineering from the Harbin Institute of Technology at Shenzhen, Shenzhen, China, in 1998 and 2007, respectively.

She is currently a Professor with the Center for Cognitive Technology, Shenzhen Institute of Advanced Technology, Chinese Academy of Sciences, China. She has authored or coauthored more than 60 scientific papers published in refereed journals and conference proceedings. Her research interests include parallel robots, medical assistant robots, and mobile robots.

**BING LI** (SM'16) received the Ph.D. degree from The Hong Kong Polytechnic University, Hong Kong, in 2001.

He was a Professor of mechatronics, in 2006. He is currently the Head of the School of Mechanical Engineering and Automation, Harbin Institute of Technology at Shenzhen, China. His research interests include parallel manipulators and control, mechanical vibration and control.

Dr. Li is an Associate Editor of the *International Journal of Mechanisms and Robotic Systems*.

**JIANWEI ZHANG** (M'91) received the B.S. and M.S. degrees from the Department of Computer Science, Tsinghua University, Beijing, China, in 1986 and 1989, respectively, and the Ph.D. degree from the Department of Computer Science, Institute of Real-Time Computer Systems and Robotics, University of Karlsruhe, Karlsruhe, Germany, in 1994.

He is currently a Professor and the Head of the TAMS Group, University of Hamburg, Hamburg, Germany. He has published more than 200 journal and conference papers, technical reports, four book chapters, and two research monographs. His research interests include multimodal perception, robot learning, and mobile service robots.

Dr. Zhang received several awards, including the IEEE ROMAN and IEEE AIM Best Paper Awards.